Close-packed dual-color micro-LEDs enable cortical-layer-specific bi-directional *in vivo* optogenetic electrophysiology

Dacheng Mao[1,4], Feng Sun[1,4], Bradley Driscoll[2,4], Zhihao Li[1], and Guangyu Xu[1,3,5,*]

[1]Department of Electrical and Computer Engineering, University of Massachusetts, Amherst, MA 01003, USA
[2]Department of Phycological and Brain Sciences, University of Massachusetts, Amherst, MA 01003, USA
[3]Department of Biomedical Engineering, University of Massachusetts, Amherst, MA 01003, USA
[4]These authors contributed equally to this work.
[5]Lead contact
[*]Correspondence: (email) guangyux@umass.edu (G.X.)

SUMMARY

Optogenetics promises to manipulate the brain circuitry by exciting or inhibiting the same neurons via different colors of light (i.e., bi-directionality), and furthermore co-works with electrophysiology for low-crosstalk, high-resolution probing of the brain. Limited by feasible integration methods though, neural probes with close-packed dual-color light sources remain underdeveloped, making high-resolution bi-directional *in vivo* optogenetic electrophysiology technically challenging. Here we report, based on heterogeneously stacked III-V epitaxial films, a monolithic neural probe integrated with close-packed dual-color micro-LEDs and microelectrodes in 20 and 50 μm pitches, respectively. The resulting devices enable bi-directional *in vivo* optogenetic electrophysiology across layers IV and V of mouse somatosensory cortex, where dual-color LEDs are observed to excite and inhibit layer-specific brain dynamics. Such inter-layer bi-directional *in vivo* optogenetic studies, in which our scalable probes are well suited, can add to high-resolution interrogation of the brain circuitry and shed light on animal disease models.

INTRODUCTION

Optogenetics, a method to optically control cell activity via light-sensitive proteins[1,2,3], has risen to the focus of the neuroscience community for its combined advantages on temporal precision[2,4], cell-type specificity[3,5], and bi-directionality[6,7,8] (i.e. enhance or suppress neural activity upon the color of light). The capability of bi-directional neuromodulation not only offers an alternative approach to dissect heterogenous brain circuits[2,9,10] but also holds promise to develop therapeutic interventions[9,11,12](e.g. inhibiting epilepsy). Yet, the dual-colored light required for bi-directional optogenetic control of the same neurons (colocalized modulation[13]) often occupies a broad optical bandwidth[6,7,14] hindering its capability to co-work with fluorescent live cell imaging to examine optogenetic effects in a low-crosstalk manner[15]. For instance, microscopy or fiberscope based all-optical approaches were often to combine calcium/voltage imaging with single-colored (unidirectional) optogenetic control of the cells[16,17,18,19]. In this perspective, optogenetic electrophysiology[20,21], a powerful approach that shares the benefits of high-resolution electrical recording and high-precision optical manipulation of cells[22,23,24,25], is possible to circumvent the bandwidth limitation of all-optical methods and trace real-time brain dynamics under bi-directional optogenetic patterns with low cross-talk[23,25] (note: behavioral studies have also been successful to test colocalized bi-directional optogenetic effects[13], but challenging to trace their neural basis with high temporal precision).

To make full impact of optogenetic electrophysiology, it would be ideal to build implantable neural interfaces that can output different colors of light with high spatial resolutions and include arrays of microelectrodes (i.e. MEA) for neural recording, which could be used to precisely map the functional circuits in the brain[2,10], and ultimately develop animal disease models[9,11]. To date, a variety of optoelectronic neural probes assembled with light sources (either passive[26,27] or

active[22,28] ones) and microelectrodes have been applied to optogenetically modulate neural activities at various regions of the brain. Among them, single-colored micro-LED-based probes were noted for their spatial resolution[22], scalability[29], and power consumption[22], and have been optimized to minimize their photovoltaic artifact on neural recording[23]. Yet, limited by feasible integration methods[22,30,31], probes with high density arrays of dual-color light sources are still missing, making high-resolution bi-directional *in vivo* optogenetic electrophysiology technically challenging. This is a non-trivial task as it requires monolithic integration of different types of active light materials[32] that can be patterned into a small footprint adjacent to low-artifact microelectrodes[23,25], all of which need to be highly scalable[22] and compatible with the following deep etching steps to form a sub-100 μm-thick shank[22,33].

To address this unmet need, here we report a monolithic neural probe based on heterogeneously stacked III-V epitaxial films, where close-packed dual-color micro-LEDs and microelectrodes are placed in 20 and 50 μm pitches, respectively. Both blue and red LEDs feature high brightness, small spot size, fast response, and low voltage operation, whereas the microelectrodes are coated with a poly(3,4-ethylenedioxythiophene) polystyrene sulfonate (PEDOT:PSS) layer for high-fidelity neural recording[34,35]. The resulting high-yield devices demonstrate their use for bi-directional *in vivo* optogenetic electrophysiology across layers IV and V of mouse somatosensory cortex, where dual-color LEDs are observed to excite and inhibit brain dynamics in a cortical-layer-specific manner, possibly due to interlayer signaling pathways[36,37,38]. Such layer-specific bi-directional *in vivo* optogenetic studies enabled by our scalable probes may add to high-resolution interrogation of the brain circuitry[2] and ultimately shed light on neurological disease models[9].

RESULTS

Design of the probe structure

In bi-directional optogenetic studies, the activation spectra of excitatory and inhibitory opsins need to be well separated from each other to minimize their optical crosstalk[6,14]. For this reason, here we chose to use *Chrimson*[39] and *GtACR2*[40] as excitatory and inhibitory opsins, respectively, which have shown their low crosstalk in bi-directional optogenetic experiments[13,14]. Furthermore, these two opsins have been fused together into *AAV-BiPOLES* vectors, allowing *both* of them to be delivered to the same cortical neurons by single AAV-virus injection[14]. To optically activate *GtACR2* and *Chrimson*, on the hardware side we chose to build GaN- and AlGaInP-based micro-LEDs (i.e. blue and red LEDs), which can output 462/19 nm and 625/10 nm light that fall in the activation spectra of these two opsins, respectively[14,39,40]. This approach of building dual-color LEDs is intended to leverage commercial epitaxial GaN-on-Si and AlGaInP-on-GaAs wafers, which were known to offer bright, stable, and scalable LED arrays[22,31,41].

While blue and red LEDs can be separately built in a high-density array form[22,41,42], integrating both of them monolithically on the same probe is the key for high-resolution bi-directional optogenetic studies. Here we chose to achieve this by physically transferring the epitaxial layers (i.e. epilayer) of an AlGaInP-on-GaAs wafer on top of the GaN-on-Si wafer, with a SU8 film placed in between to bond these epilayers. These heterogeneously stacked epilayers readily lend themselves to high yield fabrication of red LEDs on top of blue LEDs, allowing for their monolithic integration (Figure 1A).

On the neural recording end, the MEA needs to lower its electrode impedance to obtain a high signal-to-noise-ratio (SNR) during optogenetic experiments[35,43]. For this reason, we chose to build an Au-based MEA electroplated with a PEDOT: PSS layer, which is known to effectively reduce

the electrode impedance[34,35] (Figure 1B). This electroplating step reduces the electrode impedance across the entire MEA (see the subsequent sections), although non-uniform coating of the PEDOT:PSS layer may occur on some electrodes[44].

Finally, to allow for high-resolution optogenetic electrophysiology across cortical layers, we chose to build *both* dual-color LEDs *and* microelectrodes in close-packed arrays along different access depths of the probe. For this reason, our neural probe is designed to have 8 groups of dual-color LEDs closely packed in a 50 μm vertical pitch. Each group is composed of 2 blue and 2 red LEDs placed in a 20 μm pitch, with all LEDs being 7 μm-by-7 μm in size. A total of 17 recording electrodes with 20 μm-by-20 μm in size are placed next to these 8 groups of dual-color LEDs (Figure 1B). Moreover, we chose to place these electrodes along two edges of the shank structure, which has been recommended to record spikes with larger amplitudes (vs. placing them near the center of the shank[45]). The resulting LEDs and electrodes cover *ca.* 380 μm vertical scan at the probe tip, which was designed to conduct optogenetic electrophysiology across different cortical layers in the mouse brain[38,46] (Figures 1C and S1).

Fabrication and packaging of the monolithic probe

With the foregoing design considerations, we started our probe fabrication by patterning an 8-by-2 cross-barred blue micro-LED array on a GaN-on-Si wafer using a similar approach as we reported before[42] (Figure 1D). These blue LEDs are placed in a horizontal/vertical pitch of 20/50 μm, contacted by a Ni/Au current spreading layer to lower their turn-on voltage[22], and passivated by a plasma-enhanced chemical vapor deposition (PECVD) based SiO_2 layer. The resulting array was spin coated with a SU8 layer, followed by a soft baking step, which later serves to bond the epilayers from the AlGaInP-on-GaAs wafer.

On the other end, we applied wet etching to remove the GaAs substrate from AlGaInP-on-GaAs wafer, leaving 5-6 μm thick epilayers (consist of AlGaInP-based quantum well layers[32]) floating in the etchant. We then used a pipette to suck the epilayers out of the etchant, rinsed them with DI water, and placed them on the soft-baked SU8 layer coated on blue LEDs. Afterwards, the resulting device sequentially went through a *ca.* 20 min drying step in a desiccator, a UV exposure step to cross-link the SU8, and a 30 mins hard-baking step for permanent bonding of the epilayers. Importantly, such heterogeneously stacked epilayers allow us to pattern an 8-by-2 cross-barred red LED array using the same approach as we used to form the blue LED array, with the red and blue LED pixels being closely packed to each other. The resulting dual-color LEDs were passivated with a *ca.* 5 μm thick SU8 layer, which later serves to lessen the electromagnetic interference (EMI) of the neural recording traces[23].

On top of the passivated dual-color LEDs, we patterned an Au-based MEA and passivated it with a stack of SiO_2 (by sputtering) and SU8 layers. The resulting electrodes are 20 μm-by-20 μm in size and placed with a vertical pitch of 50 μm on both sides of the dual-color LEDs. Similar to the approach used to form silicon neural probes[22,33], we next applied deep reactive ionized etching (DRIE) steps from both the front and back sides of the device to define the horizontal dimension and the thickness of a shank structure, respectively (see details in Methods). The resulting shank (contains dual-color LEDs and the MEA) is *ca.* 200 μm in width, 5 mm in length, and 50 μm in thickness, representing the completion of the monolithic probe fabrication.

Lastly, we wire-bonded the as-made shank onto a printed circuit board (PCB) and encapsulated it with UV-curable epoxy. These packaging steps allow us to electroplate the MEA with a PEDOT: PSS layer as we reported before[44], which prepares our probes for subsequent experimental use.

Optoelectronic performance of the neural probe

To examine if the packaged probes suffice high-resolution *in vivo* bi-directional optogenetic electrophysiology studies, we next characterized the optoelectronic performance of the dual-color LEDs and the PEDOT:PSS-coated MEA as detailed below.

To enable *in vivo* optogenetic control within specific cortical layers, both blue and red LEDs are required to output bright, localized, and fast-switching light, ideally in a low-voltage operation[13,22,29,42]. To this end, we first measured the optical power density ($P_{blue/red}$) and the spatial profile of the illumination spot (I_{light}) of each LED pixel as we reported before[42]. When biased at an injection current (I_{LED}) of 9 [20] μA, blue [red] LED pixels readily show high brightness with $P_{blue/red}$ ~ 4 mW/mm^2 (Figures 2A and 2B), which falls into the range required for *in vivo* optogenetic control over neural activity via *GtACR2* [*Chrimson*][14,39,40]. While the difference of I_{LED} between blue and red LEDs did exist (likely due to different epilayers and contact resistances), it is encouraging to note that such high brightness is achieved with the driving voltage across each pixel (V_{LED}) being *ca.* 3.5 V [7 V] for blue [red] LEDs. Such low-voltage operation leads to 31.5 [140] μW electrical power dissipation per blue [red] LED pixel, which has been deemed suitable for *in vivo* use[22,47]. Moreover, we note that the full width at half maximum (FWHM) of the LED light spot is typically *ca*. 10 μm at the probe surface with I_{LED} ranging from 2 to 10 [5 to 25] μA in blue [red] LEDs (Figure 2C, the FWHM is overestimated here as the center of the light spot saturates the camera). Such localized light output is essential for bi-directional optogenetic control within specific cortical layers, whose thicknesses are *ca.* 100 μm in mice[38,46]. Finally, we found that such bright, localized pixel output can be pulsed with a 10 ms-duration at up to 40 Hz pulsing frequencies (Figure 2D). Each pulse featured *ca.* 2 ms rising and falling times, suitable for temporally precise neurostimulation[4]. These results suggest that our dual-color LEDs meet the

brightness, resolution, and speed requirement for *in vivo* bi-directional optogenetics within specific cortical layers.

To assess the performance of our MEA for high-SNR recording, we next conducted electrochemical impedance spectrometry (EIS) and cyclic voltammetry (CV) testings of all 17 electrodes using the approach we reported before[44]. Our results show that the PEDOT:PSS layer was effective in altering the EIS (from 0.1 to 100 kHz) and CV (from -0.6 to 0.8 V) data measured from the MEA (Figures 2E-2G). First, after the electroplating step, all 17 electrodes dropped their EIS impedance amplitude at 1 kHz from 3.07 ± 0.55 MΩ to 44 ± 3.76 kΩ (although non-uniform coating on some electrodes may occur, Figure 1B), and increased their EIS phase in the entire frequency range. This result suggests that the PEDOT:PSS layer effectively reduced the electrode impedance, and changed the electrodes to be less capacitive (i.e. away from -90° phase). Second, the PEDOT:PSS coating step increased the current values in the CV curves by *ca.* one order with no apparent redox peaks. This result suggests that the PEDOT:PSS layer effectively augmented non-Faradaic charging processes, likely because its roughness and porosity increased the effective surface area of the electrode, and thus decreased the electrode impedance[44]. For these reasons, our low-impedance, non-Faradaic MEA lends itself to high-SNR *in vivo* neural recordings.

Strategies to suppress the recording artifact

Before performing *in vivo* optogenetic studies, we also need to examine if our low-impedance MEA could feature low recording artifact[23,25] for the sake of high signal-to-background ratio (SBR)[44]. In fact, SNR and SBR have been recognized as two equally important figures-of-merits to achieve high-fidelity neural recording[23,25]. Furthermore, the recording artifact has been concerning in monolithically integrated neural probes, where the neural recording could be

impacted by EMI-induced, photovoltaic-induced, or residual artifacts[23]. For these reasons, it is essential to evaluate if the pulsing of LEDs (required for optogenetic testing) will cause non-negligible artifacts in the recording traces, and figure out strategies to suppress them.

To quantify the amplitude of the recording artifact, we immersed the probe in 1 x Dulbecco's phosphate-buffered saline (DPBS) solution, and applied a single 50 ms voltage pulse to transiently turn on and off single LED (V_{high} is *ca.* 3.5 V [7 V] in blue [red] LED). Such pulsing operation of LEDs was intended to emulate the illumination pattern and light brightness used in optogenetic studies. It fluctuated the voltage traces of all 17 electrodes that were bandpass (BP) filtered at 250 Hz – 10 kHz, mainly near the rising/falling edges of the pulse with a duration of < 4 ms. The mean peak-to-peak magnitude (V_{pp}) of these traces is taken as the artifact amplitude (Figure 3A).

Subsequently, we took two strategies suggested in literature to mitigate the recording artifact[23] (Figures 3A and 3B). First, we added a 0.1 μF capacitor in parallel to the output of the source-measurement unit (SMU) used to pulse the LEDs. This approach serves to low-pass (LP) filter the voltage pulses and slows down the LED switching (from 50 μs to 2.5 ms). The resulting artifact amplitude was significantly reduced by 90%, likely due to the removal of high-frequency artifacts. Second, with this LP capacitor being connected, we elevated the off-state voltage of the LEDs (V_{low}) from 0 to the near-threshold value of the select LEDs (2.5 V [3 V] for blue [red] LEDs). This approach serves to cut the voltage ramping on LEDs and reduce the capacitive coupling to recording traces, resulting in an additional *ca.* 10% drop of the artifact amplitudes. Together, such LP filtered, V_{low} adjusted pulsing of blue [red] LEDs readily leads to 100 [200] μV of artifact with sub-2 ms duration (Figure 3C), which is on par with other LED-integrated neural probes used for optogenetics[23]; the larger voltage swing (i.e. V_{high} - V_{low}) applied to red LEDs may result in larger EMI-related artifacts compared to those in blue LEDs. Taking one step further, our data show that

simultaneously illuminating more LED pixels does not necessarily increase the artifact amplitude (Figure 3D). This result suggests that our recording artifact largely comes from EMI across leading wires rather than the photovoltaic effect[23]. Nonetheless, the mitigated artifact amplitudes in some electrodes were still non-negligible near the rising/falling edges of the LED pulses (Figure S2), which need to be excluded from the traces for artifact-free analysis.

Last but not least, we noted that driving LEDs with a sinusoidal voltage waveform can further reduce the artifact[22]. This approach however is unable to keep LEDs at their maximum $P_{\text{blue/red}}$ in the entire pulse window. We thus chose to drive LEDs with LP-filtered square pulses in this work.

Bi-directional *in vivo* optogenetic electrophysiology with packaged monolithic probes

After *in vitro* testing of the probe performance and the recording artifact, we next applied our dual-color neural probes to the cortex layers of anesthetized mice to assess their capabilities for bi-directional *in vivo* optogenetic electrophysiology. Specifically, *AAV-BiPOLES-CaMKII* vectors were injected to the cortical regions of the mice (Methods), which allows *Chrimson* and *GtACR2* opsins to express in the excitatory neuron populations across the primary somatosensory cortex (S1)[14]. Followed by 3 weeks of recovery and viral expression, the neural probe was inserted into the brain of head-fixed, anesthetized mice (Methods), with the LEDs and electrodes being located across layers IV and V in the S1 region (examined by the brain slice image taken after *in vivo* testing, Figure S3). These two layers were chosen in our studies since they play vital roles in forming the circuit pathways of sensory perception and controlling the sensory responses[37,46,48]. Since each layer spans *ca.* 200 – 300 μm in depth[38,46], we can access them separately by illuminating *either* the top *or* the bottom 3 rows of LEDs (with a total of *ca.* 380 μm vertical span) on the probe, and record the neural activity in *both* layers using the MEA.

We then conducted bi-directional optogenetics electrophysiology in one animal by sequentially pulsing 6 red and 6 blue LEDs located in layer V (red [blue]: seven 2-s periods with $t_{off/on/off}$ = 0.5/0.05/1.45 s [$t_{off/on/off/on}$ = 0.5/0.5/0.5/0.5 s]; we chose to always pulse blue LEDs with a longer t_{on} to enhance the inhibition effect; temperature changes under these pulsing conditions were estimated to be < 1 ºC, see Figure S4), with the MEA traces being BP-filtered at 250 Hz – 10 kHz to detect neural spiking events (Methods; Figure S5A); each 2-s period is defined as a trial here. To conduct artifact-free analysis of the recorded traces, we first excluded the 4-ms of data centered at the rising/falling edges of each LED pulse (Figure S2). The rest of the traces were then used to extract spikes whose negative amplitudes are >5 times the noise floor (Figure 4A and Methods). Next, for each electrode, we pooled spikes recorded in 7 trials for principal component analysis (PCA), and applied density-based spatial clustering of applications with noise (DBSCAN) to sort spikes[49,50,51] (Figure S6). It is noted that our sorted spike waveforms (excluding noises) were often with a sub-500 μs trough-to-peak duration (Figures 4B and S7A), suggesting their possible origins from fast-spiking interneurons near the MEA (e.g. parvalbumin-expressing (PV) neurons)[52,53,54,55]. Such interneuron activities may be evoked by optogenetically controlled excitatory neurons (opsins were expressed in excitatory neurons via the *CaMKII* promoter[14]) via local circuit[36,46,49]. The activity of excitatory neurons (typically with > 500 μs durations)[52,53,54], on the contrary, was not as significant here, likely because they were further distance away from the MEA or in turn inhibited by connected interneurons.

To quantify the optogenetic effect of pulsed LEDs, we plotted the spike timing during seven 200-ms windows, one from each 2-s trial (Figures 4C-4E, data were aligned by red or odd numbered blue LED pulses), followed by summing spike count from 16 electrodes (one electrode failed in experiments) in these 7 windows to yield peristimulus time histograms (PSTH, Figure

4E). Moreover, we compared spike count recorded at each electrode within [0, 100 ms] and [-100 ms, 0] windows to examine LED-induced optogenetic effects across the MEA (Figures 4F and 4G). After *in vivo* recording, we collected brain slices to examine the probe position across cortical layers by imaging (Figure S3).

Our data show that, when neurons were illuminated by 6 red LEDs, the spike count across the MEA was increased by 55 ± 32% (top row in Figures 4E-4G). This result may originate from additional depolarization of excitatory neurons via the red-light activation of *Chrimson*[39], which leads to more frequent spiking of their projected interneurons nearby during each red-LED pulse. On the other hand, when neurons were illuminated by 6 blue LEDs, the spike count across the MEA was decreased by 30 ± 11% (bottom row in Figures 4E-4G). This result may originate from additional hyperpolarization of excitatory neurons via the blue-light activation of *GtACR2*[40], which leads to less frequent spiking of their projected interneurons nearby during each odd-numbered blue LED pulse. In sum, the contrast between these two sets of data evidently suggests the capability of our probe for bi-directional *in vivo* optogenetic electrophysiology studies.

Layer-specific bi-directional optogenetic control over whisker-evoked neural activity

After showcasing the capability of our probe for bi-directional optogenetic electrophysiology, we took one step further to investigate if they can bi-directionally alter the sensory responses to whisker stimulation across layers IV and V (with the probe being inserted in the same position as in Figure 4). Here our work targeted to the whisker system as it is a preferred cortical model for mechanistic studies of sensory processing[56,57]. Specifically, we deflected mouse whiskers (from the same animal used in Figure 4) contralateral to the brain region we inserted the probe by pulsing a current-driven solenoid actuator (1st row in Figures 5A and S5B, seven 2-s periods with $t_{off/on/off}$

= 0.5/0.01/1.49 s, each 2-s period is defined as a trial here), and at the same time recorded the cortical responses via the MEA. Similar to methods described in Figure 4, we conducted spike sorting (excluded the 4-ms of data centered at the rising and falling edge of each whisker pulse to assure artifact-free analysis, Figure S2), generated raster plots and PSTHs (data were aligned by whisker pulses, Figures 5B and 5C), and counted spikes in each electrode (Figure 5D). Similar to previous works[46,58], our data show that whisker deflections readily evoked sensory responses across layers IV and V ([-100 ms, 0] vs [0, 100 ms] windows: 40 vs 157, 1st row in Figure 5C). This data set our baseline to analyze the following experiments when *both* whisker stimulation *and* LED illumination were applied.

After testing the sensory responses to whisker stimulation alone, we next combined whisker stimulation and LED illumination together to investigate if dual-color LEDs can optogenetically modify whisker-evoked sensory responses in a bi-directional manner. To achieve this goal, we started by pulsing 6 red LEDs positioned in layer V (2nd row in Figure 5A; seven 2-s periods with $t_{off/on/off}$ = 0.51/0.05/1.44 s), with each red LED pulse following right after a 10-ms whisker pulse (in this configuration, whisker stimulations are still offered in seven 2-s periods with $t_{off/on/off}$ = 0.5/0.01/1.49 s, Figure S5B). To study the layer specificity, we then conducted the same set of experiments by illuminating 6 red LEDs positioned in layer IV (1st row in Figure S8A).

Following the same data analysis as described above, we found that illuminating red LEDs positioned in *either* layer further enhanced the neural activity across layer IV and V compared to the whisker-stimulation-alone experiment, evidenced by an increase of the total spike count ([0, 100 ms] window from all 7 trials) across 16 electrodes (Figures 5B-5E and S8B-S8E). This result reaffirms the optogenetic excitation effect of red LEDs observed in the LED-only experiment. On the layer-specificity end, we found that illuminating red LEDs in layer IV was more effective to

enhance whisker-evoked neural activity than illuminating those in layer V (444 ± 86% vs 266 ± 37%, Figure 5F). This result reaffirms the heterogeneity of cortical circuits and the need for high-resolution neuromodulation with close-packed micro-LEDs. Such layer specificity may relate to the signaling pathways from layer IV to layer V in the S1 region, where layer IV could act as the upstream of other cortical layers in forming the interlayer circuitry[36,37,38]. If this were the case in our experiments, red-LED-illuminated excitatory neurons in layer IV may activate downstream interneurons (e.g. PV neurons) across both layers via synaptic projections, resulting in a stronger optogenetic excitation effect. Finally, we observed that illuminating 3 red LEDs in either layer can sufficiently enhance whisker-evoked neural activity, suggesting that our close-packed LEDs can offer optogenetic control at high spatial resolution (Figures 5F, S8 and S9).

We further our study by similarly examining the optogenetic effect of blue LEDs on whisker-evoked neural activity in layers IV and V. Here we chose to pulse 6 blue LEDs positioned in *either* layer IV *or* layer V (4^{th} row in Figure S8A and 3^{rd} row in Figure 5A; seven 2-s periods with $t_{off/on/off/on}$ = 0.5/0.5/0.5/0.5 s), with each odd-numbered blue LED pulse started together with a 10-ms whisker pulse (in this configuration, whisker stimulations are still offered in seven 2-s periods with $t_{off/on/off}$ = 0.5/0.01/1.49 s, Figure S5B).

Following the same data analysis as described above, we found that illuminating blue LEDs positioned in *either* layer will overall inhibit the neural activity across layer IV and V compared to the whisker-stimulation-alone experiment (Figure 5G), evidenced by a decrease of the total spike count ([0, 100 ms] window from all 7 trials) in the majority of 16 electrodes (Figures 5E and S8E), This result reaffirms the optogenetic inhibition effect of blue LEDs observed in the LED-only experiment (Figure 4). On the layer-specificity end, we noted that illuminating blue LEDs in layer V decreased the whisker-evoked spike count more uniformly across the MEA than

illuminating those in layer IV (-26 ± 22% vs -22 ± 40%, Figures 5E, G and S8E; their mean values were similar). This is likely because blue-LED-illuminated excitatory neurons in layer IV may inhibit interneurons across both layers (e.g. somatostatin-expressing (SST) neurons)[36,37,38]. Inhibiting these interneurons may effectively weaken the inhibition (and thus increase the activity) of their downstream interneurons (e.g. PV neurons)[59,60,61], which may result in an increase of spike counts near some electrodes. Such effect could be less significant when layer V was illuminated by blue LEDs, since the optogenetic effect may influence fewer interneurons (largely located in layer V).

DISCUSSION

We have presented a monolithic neural probe integrated with close-packed dual-color micro-LEDs and microelectrodes, aiming for high-resolution bi-directional optogenetic electrophysiology. Bright, localized, and fast-pulsed light from LED pixels, combined with low-impedance, low-artifact MEA, powers bi-directional *in vivo* optogenetic electrophysiology studies across cortical layers in anesthetized mice. Using our probes, we were able to observe layer-specific bi-directional optogenetic control over whisker-evoked neural activity in layers IV and V, which suggests the heterogeneity of cortical circuits and the need of high-precision neural interfacing with these close-packed dual-color LEDs. It can also be interesting to further study the relevance between interlayer signaling pathways and optogenetic effects on neurocircuits, which can be highly related to local populations of different cell types (see results from another animal, Figures S7 and S9).

Such bi-directional, interlayer optogenetic electrophysiology enabled by our probe may add to high-resolution functional mapping of the brain circuitry, particularly those involving interlayer neurocircuits[36,37] or highly heterogenous cortical regions[29,43]. Leveraging their scalability, these

probes can be tailor designed with suitable LED or MEA pitches/counts for targeted science problems, or extended into multi-shank neural probes for accessing more cortical areas[22,33]. Besides cortex dynamics, the length of our probes (*ca.* 5-mm) can also lend themselves for deep brain access[11]. For instance, combining with population-specific opsin expression[3,4], our probes may offer bi-directional control over local circuits or individually excite two neuronal populations in the deep brain, which can help develop animal disease models at high precision[9] (e.g. Parkinson[11], epilepsy[26]).

Finally, we remark a few steps to further optimize the probe performance and the experimental design. First, the EMI-induced recording artifact in our probe is partially alleviated by the SU8 layer placed between LED and MEA layers, whose 5 μm thickness lessens the capacitive coupling during MEA recording. Moving forward, this EMI artifact should be further reduced by adding a metallic shielding layer between LED and MEA layers[23]. Second, the red LEDs presented in this work still suffered from higher drive voltages than blue LEDs. To solve this issue, we could work to reduce both contact and series resistances of red LEDs by forming n-contacts on top of an ohmic contact layer (via adjusting the etching time/methods). Third, our probes can currently maintain their performance in the electrophysiology environment for *ca.* 3 weeks (Figure S10). Their chronic stability could be further improved by passivating the device with alternative waterproofing materials (e.g. Parylene C)[43,62,63]. Fourth, to further improve the spatial resolution of LED-based *in vivo* optogenetic control (e.g. down to cellular levels), one may consider integrating a microlens array on top of LEDs to spatially confine their emission patterns in the tissue[64,65]. Fifth, our tethered probing system (including the PCB) is miniaturized (sub-500 mm^3) and light-weighted (sub-2g), which can be applied to freely moving animals in a limited space. A

tetherless probing system would require further development of high-bandwidth wireless transceiver chips to be assembled on the PCB[13,66].

EXPERIMENTAL PROCEDURES

Resource availability

Lead contact

Further information and requests for resources should be directed to and will be fulfilled by the lead contact, Guangyu Xu (guangyux@umass.edu).

Material availability

This study did not generate new materials.

Data and code availability

The raw data are available from the lead contact (guangyux@umass.edu) upon reasonable request.

Probe fabrication and packaging

A cross-barred blue LED array was fabricated on a commercial epitaxial GaN-on-Si wafer (Enkris Semiconductor) using a similar approach as we reported before[42], except that here we applied a Ni/Au (7/10 nm) current spreading layer onto the p-GaN to further reduce the contact resistance[22] (Figure S11 and S12). Specifically, we chose Ti/Al/Cr/Au layers (10/70/10/120 nm), an indium tin oxide layer (ITO, 120 nm), and Cr/Au layers (10/120 nm) to serve as n-, p-, and pad-contacts, respectively[67]. After passivating the array with a PECVD-SiO_2 layer (*ca.* 200 nm), we spin coated a SU8 layer (*ca.* 5 μm) on top and soft baked it at 95 ºC for 10 mins.

On the other end, we immersed an AlGaInP-on-GaAs wafer (Powerway Wafer, Figure S13) in NH_4OH:H_2O_2 = 1:6 to separate AlGaInP epilayers (*ca.* 5.86 μm) from the GaAs substrate[32]. This wet etching step completely removed the GaAs substrate (*ca.* 350 μm) and stopped at the Si-GaInP etching-stop layer (171 nm). We then used a pipette to transfer these separated epilayers

from the etchant to the DI water, rinse them 3 times with fresh DI water, and placed them on the soft-baked SU8 layer coated on the blue LED array with the c-GaP layer (p-contact of red LEDs) facing up. These epilayers were permanently bonded to SU8 by drying the device in the desiccator, cross-linking SU8 via UV exposure, and a hard-baking step (200 ºC for 30 mins). A slow temperature ramping process (*ca.* 10 ºC/min) was applied to prevent the radical flow of the SU8 underneath the epilayers. Next, a cross-barred red LED array was fabricated on the epilayers using the similar approach as the blue LED array. Specifically, we chose Cr/Au layers (40/120 nm), an ITO layer (120 nm), and Cr/Au layers (40/120 nm) to serve as n-, p-, and pad-contacts, respectively[41]. The entire array was then passivated by PECVD-SiO_2 (*ca.* 200 nm) and SU8 (*ca.* 5 μm) layers.

On top of the passivated dual-color LEDs, we fabricated a Cr/Au-based (10/50 nm) MEA with Cr/Pt/Cr/Au layers (10/50/10/120 nm) as pad-contacts. The resulting device was passivated by sputtered SiO_2 (*ca.* 10 nm) and spin-coated SU8 (*ca.* 5 μm) layers, followed by a wet etching step (diluted buffered oxide etchant, 1:50) to open the electrode and pad areas.

On the front side of a LED-MEA integrated device, we formed a 250 μm-wide trench region surrounding the designed shank structure by a series of RIE steps[33], which served to remove SiO_2/SU8 /GaN layers in the trench (patterned by a 12 μm photoresist layer) and stopped at the Si substrate. We then applied a DRIE step to remove 80 μm thickness of Si in the trench, which helped to define the final thickness of the probe (*ca.* 50 μm) while leaving *ca.* 30 μm over-etch tolerance during the following back-side thinning step. Next, a photoresist layer (*ca.*12 μm) was patterned on the back side of the device, followed by thinning down the Si substrate by *ca.* 750 μm using another DRIE step. This step formed a *ca.* 50 μm thick probe structure and separated the probe from the bulk of the wafer.

A custom-made PCB was soldered with cable connectors (Molex, product no. 5051102091) and stainless wires (A-M Systems, catalog no. 791900) to serve as the reference/ground electrodes (*ca.*1 cm length of the PFA coating was removed). Lastly, we wire-bonded the probe onto the PCB and encapsulated the bonding wires with a UV-curable epoxy (Epoxies, Et 60-7159).

Electroplating and MEA characterization

Using the same approach as we reported before[44], we used a potentiostat (Gamry, Reference 600+) to sequentially electroplate PEDOT:PSS layers on individual electrode, followed by EIS and CV tests with a three-electrode configuration.

LED characterization

Using the same approach as we reported before[42], we applied a current bias to each LED pixel by a SMU (Keysight B2902A), and measured its optical power by an optical power meter (Thorlabs PM100D). The wavelength correction was set to 462 nm [625 nm] for blue [red] pixels to match its dominant photoluminescence wavelength. The measured power was divided by the pixel area (49 μm^2) to obtain the optical power density. The I-V characteristics, spatial profile of the output light, and pulsed switching for each LED pixel were measured by the SMU and/or an upright microscope (Nikon FN1). We also estimated the temperature change near pulsed LEDs using a thermal imager (FLIR Photon 320), with LEDs being left in air or inserted into a brain phantom (2% agarose in artificial cerebrospinal fluid, see Figure S4).

Artifact characterization

Using two flat flexible cables (FFC, SAMTEC, FJH-20-D-31.75-4), we connected LEDs and the MEA on the probe to a LED driving circuit and an electrophysiology amplifier chip (RHD2164, Intan technologies), respectively. The former includes the SMU for biasing the LED pixel and a microcontroller (Arduino UNO, powered by Keysight E36312A) for pixel selection (Figure S14); the latter is wired to an Intan chip interface board for controlling the cell recording. The SMU and the microcontroller were programmed in the Matlab platform (Mathworks); the list sweep function in the SMU can output a half-cycle sinusoidal signal with a 50-ms period.

To quantify the recording artifacts, we immersed a packaged probe (together with its reference and ground electrodes) in the 1x DPBS (Thermofisher) solution. We then pulsed the select LEDs and simultaneously collected the recording traces. The recording signals were sampled at 20-kHz and bandpass filtered at 250 Hz–10 kHz; the 60-Hz noise and dc offset were removed by built-in filters of an Intan RHD USB interface software (Intan Technologies). The SMU output signal was also recorded by the Intan chip to synchronize the LED illumination patterns with the recording traces. The recording artifacts were quantified by the V_{pp} values in these traces.

Animal procedures

All animal procedures were approved by the Institutional Animal Care and Use Committee at the University of Massachusetts Amherst. Adult male and female wildtype C57BL/6J mice (2-3 months old, 21-30g) were used for bi-directional *in vivo* optogenetic study. Mice were group housed before surgery with food and water available *ad libitum* on a reversed 12h:12h light-dark cycle. During stereotaxic surgery, mice received 1-2.5% isoflurane anesthesia during all procedures. The body temperature was maintained at 37 °C with a Deltaphase isothermal pad and insulator. Mice were administered subcutaneous injections of carprofen and cefazolin 5 mg/kg.

AAV5 BiPOLES virus (*AAV5-CaMKII-somBiPOLES-mCerulean*; Addgene # 154948) was injected bilaterally in 500 nL volume at the site of the whisker barrel cortex[68] (AP -1.0, ML +/- 3.0 and DV -1.5). After surgery, mice were single-housed and allowed to incubate at least 3 weeks before experimentation.

To conduct *in vivo* experiments, we attached the probe-bonded PCB onto a micro positioner in a stereotaxic electrode holder to accurately insert the probe to the target brain region. The probe was zeroed at the brain surface after making the craniotomy and lowered with a speed of ~ 60 µm/min. Reference and ground electrodes were placed under the skin touching the skull. For both animals used in Figures 4, 5 and S9, the probe was inserted to a depth of *ca.* 888 µm from the brain surface[46] (AP -1.4, ML +3.5).

Immediately after *in vivo* experiments, the anesthetized mouse (isoflurane 1-2.5 %) was transcardially perfused using cold 0.9 % saline followed by 10 % neutral buffered formalin (VWR 16004-128). The brains were extracted and post-fixed in formalin overnight at 4°C, and then sunk in 20% sucrose for 24h. Afterwards, the brains were frozen in isopentane and cut into 40-µm coronal sections using a Leica CM3050 S cryostat. The serial sections floated in 1x DPBS at 4°C until mounted onto slides for imaging.

Optogenetic electrophysiology

During *in vivo* optogenetic electrophysiology studies, we pulsed select red/blue LED pixels via the SMU and simultaneously conducted neural recording via the Intan chip (see Artifact characterization). For experiments involving whisker stimulations, we used a solenoid actuator (uxcell), with a copper film attached to the plunger, to mechanically deflect mouse whiskers by applying 12 V voltage pulses ($t_{off/on/off}$ = 0.5/0.01/1.49 s) via the SMU. The actuator was set to

lightly touch the whiskers in the ready state and deflect the whiskers with a 3-mm traveling range when receiving a voltage pulse (Figures 5A and S1). A typical recording session (using the Intan chip with the same configuration in artifact characterization) contains one or two 14-s LED pulsing periods, some of which were paired with whisker stimulation.

Data analysis

Our data analysis was performed with custom-written programs in Matlab (Mathworks). For spike sorting, we first removed the 4-ms of data centered at each rising/falling edge of the LED/whisker pulse (Figure S2). From the rest of the traces, we detected all recorded spikes (with a 1.5 ms spike-detection interval, i.e. dead time[69,70,71]) whose negative amplitudes were >5 times of the noise floor (measured from the 1-s data prior to the 1st whisker pulse/LED pulse), and aligned them by their negative peaks.

Afterwards, for each electrode, the detected spikes from all 7 trials were pooled together for a two-dimensional PCA, followed by DBSCAN for spike sorting, Figure S6). Specifically, we set the minimum number of points in each cluster as 4 according to rule of thumb[72]; the maximum point-to-point distance within each cluster is set as the y-axis value in a k-distance curve when the slope is *ca.* 50 (chosen to balance the number of spikes and their similarity in each cluster). The sorted clusters (excluding the noise) were pooled together for the following analysis.

Spike raster plots and PSTHs were generated with a 1.5-ms temporal resolution (i.e. bin size). The latter were generated by summing sorted spikes from all active electrodes in all 7 trials.

Statistical analysis

Statistical analysis in Figure 5 was based on Student's *t*-test (two-tailed, paired-sample *t*-test).

SUPPLEMENTARY INFORMATION

Document S1. Figures S1 – S14.

Supplementary information can be found online at www.cell.com/cell-reports-physical-science.

ACKNOWLEDGMENTS

The authors are grateful for the support of this research by the National Science Foundation under contracts ECCS-1835268, 2046031, and 2055457. We thank D. E. Moorman, A. Arbabi, and Y. Sun for technical assistance.

AUTHOR CONTRIBUTIONS

D.M., F.S., and G.X. conceived and designed the experiments. D.M. and F. S. designed, fabricated, and characterized the neural probes. B.D. performed animal surgery, virus injection, device implantation, and brain slicing. D.M., F.S., and Z. L. performed optogenetic electrophysiology and spike sorting. F.S. performed whisker deflections. D. M. performed slice imaging. G.X. supervised the project. D.M., F. S., and G.X. analyzed the data and wrote the paper. All authors discussed the results and reviewed the manuscript.

DECLARATION OF INTERESTS

The authors declare no competing interests.

REFERENCES

1. Fenno, L., Yizhar, O., and Deisseroth, K. (2011). The Development and Application of Optogenetics. Annu. Rev. Neurosci. *34*, 389–412. 10.1146/annurev-neuro-061010-113817.
2. Boyden, E.S. (2015). Optogenetics and the future of neuroscience. Nat. Neurosci. *18*, 1200–1201. 10.1038/nn.4094.
3. Deisseroth, K. (2015). Optogenetics: 10 years of microbial opsins in neuroscience. Nat. Neurosci. *18*, 1213–1225. 10.1038/nn.4091.
4. Boyden, E.S., Zhang, F., Bamberg, E., Nagel, G., and Deisseroth, K. (2005). Millisecond-timescale, genetically targeted optical control of neural activity. Nat. Neurosci. *8*, 1263–1268. 10.1038/nn1525.
5. Fenno, L.E., Mattis, J., Ramakrishnan, C., Hyun, M., Lee, S.Y., He, M., Tucciarone, J., Selimbeyoglu, A., Berndt, A., Grosenick, L., et al. (2014). Targeting cells with single vectors using multiple-feature Boolean logic. Nat. Methods *11*, 763–772. 10.1038/nmeth.2996.
6. Han, X., and Boyden, E.S. (2007). Multiple-Color Optical Activation, Silencing, and Desynchronization of Neural Activity, with Single-Spike Temporal Resolution. PLoS ONE *2*, e299. 10.1371/journal.pone.0000299.
7. Zhang, F., Wang, L.-P., Brauner, M., Liewald, J.F., Kay, K., Watzke, N., Wood, P.G., Bamberg, E., Nagel, G., Gottschalk, A., et al. (2007). Multimodal fast optical interrogation of neural circuitry. Nature *446*, 633–639. 10.1038/nature05744.
8. Chow, B.Y., Han, X., Dobry, A.S., Qian, X., Chuong, A.S., Li, M., Henninger, M.A., Belfort, G.M., Lin, Y., Monahan, P.E., et al. (2010). High-performance genetically

targetable optical neural silencing by light-driven proton pumps. Nature *463*, 98–102. 10.1038/nature08652.

9. Tye, K.M., and Deisseroth, K. (2012). Optogenetic investigation of neural circuits underlying brain disease in animal models. Nat. Rev. Neurosci. *13*, 251–266. 10.1038/nrn3171.
10. Buzsáki, G., Stark, E., Berényi, A., Khodagholy, D., Kipke, D.R., Yoon, E., and Wise, K.D. (2015). Tools for Probing Local Circuits: High-Density Silicon Probes Combined with Optogenetics. Neuron *86*, 92–105. 10.1016/j.neuron.2015.01.028.
11. Mastro, K.J., Zitelli, K.T., Willard, A.M., Leblanc, K.H., Kravitz, A. V., and Gittis, A.H. (2017). Cell-specific pallidal intervention induces long-lasting motor recovery in dopamine-depleted mice. Nat. Neurosci. *20*, 815–823. 10.1038/nn.4559.
12. Krook-Magnuson, E., Armstrong, C., Oijala, M., and Soltesz, I. (2013). On-demand optogenetic control of spontaneous seizures in temporal lobe epilepsy. Nat. Commun. *4*, 1376. 10.1038/ncomms2376.
13. Li, L., Lu, L., Ren, Y., Tang, G., Zhao, Y., Cai, X., Shi, Z., Ding, H., Liu, C., Cheng, D., et al. (2022). Colocalized, bidirectional optogenetic modulations in freely behaving mice with a wireless dual-color optoelectronic probe. Nat. Commun. *13*, 839. 10.1038/s41467-022-28539-7.
14. Vierock, J., Rodriguez-Rozada, S., Dieter, A., Pieper, F., Sims, R., Tenedini, F., Bergs, A.C.F., Bendifallah, I., Zhou, F., Zeitzschel, N., et al. (2021). BiPOLES is an optogenetic tool developed for bidirectional dual-color control of neurons. Nat. Commun. *12*, 4527. 10.1038/s41467-021-24759-5.

15. Emiliani, V., Cohen, A.E., Deisseroth, K., and Häusser, M. (2015). All-Optical Interrogation of Neural Circuits. J. Neurosci. *35*, 13917–13926. 10.1523/JNEUROSCI.2916-15.2015.

16. Zhang, Z., Russell, L.E., Packer, A.M., Gauld, O.M., and Häusser, M. (2018). Closed-loop all-optical interrogation of neural circuits in vivo. Nat. Methods *15*, 1037–1040. 10.1038/s41592-018-0183-z.

17. Fan, L.Z., Kheifets, S., Böhm, U.L., Wu, H., Piatkevich, K.D., Xie, M.E., Parot, V., Ha, Y., Evans, K.E., Boyden, E.S., et al. (2020). All-Optical Electrophysiology Reveals the Role of Lateral Inhibition in Sensory Processing in Cortical Layer 1. Cell *180*, 521-535.e18. 10.1016/j.cell.2020.01.001.

18. Accanto, N., Blot, F.G.C., Lorca-Cámara, A., Zampini, V., Bui, F., Tourain, C., Badt, N., Katz, O., and Emiliani, V. (2023). A flexible two-photon fiberscope for fast activity imaging and precise optogenetic photostimulation of neurons in freely moving mice. Neuron *111*, 176-189.e6. 10.1016/j.neuron.2022.10.030.

19. Adesnik, H., and Abdeladim, L. (2021). Probing neural codes with two-photon holographic optogenetics. Nat. Neurosci. *24*, 1356–1366. 10.1038/s41593-021-00902-9.

20. Kim, C.K., Adhikari, A., and Deisseroth, K. (2017). Integration of optogenetics with complementary methodologies in systems neuroscience. Nat. Rev. Neurosci. *18*, 222–235. 10.1038/nrn.2017.15.

21. Grosenick, L., Marshel, J.H., and Deisseroth, K. (2015). Closed-Loop and Activity-Guided Optogenetic Control. Neuron *86*, 106–139. 10.1016/j.neuron.2015.03.034.

22. Wu, F., Stark, E., Ku, P.-C., Wise, K.D., Buzsáki, G., and Yoon, E. (2015). Monolithically Integrated μLEDs on Silicon Neural Probes for High-Resolution Optogenetic Studies in Behaving Animals. Neuron *88*, 1136–1148. 10.1016/j.neuron.2015.10.032.

23. Kim, K., Vöröslakos, M., Seymour, J.P., Wise, K.D., Buzsáki, G., and Yoon, E. (2020). Artifact-free and high-temporal-resolution in vivo opto-electrophysiology with microLED optoelectrodes. Nat. Commun. *11*, 2063. 10.1038/s41467-020-15769-w.

24. Park, D.-W., Schendel, A.A., Mikael, S., Brodnick, S.K., Richner, T.J., Ness, J.P., Hayat, M.R., Atry, F., Frye, S.T., Pashaie, R., et al. (2014). Graphene-based carbon-layered electrode array technology for neural imaging and optogenetic applications. Nat. Commun. *5*, 5258. 10.1038/ncomms6258.

25. Thunemann, M., Lu, Y., Liu, X., Kılıç, K., Desjardins, M., Vandenberghe, M., Sadegh, S., Saisan, P.A., Cheng, Q., Weldy, K.L., et al. (2018). Deep 2-photon imaging and artifact-free optogenetics through transparent graphene microelectrode arrays. Nat. Commun. *9*, 2035. 10.1038/s41467-018-04457-5.

26. Jiang, S., Patel, D.C., Kim, J., Yang, S., Mills, W.A., Zhang, Y., Wang, K., Feng, Z., Vijayan, S., Cai, W., et al. (2020). Spatially expandable fiber-based probes as a multifunctional deep brain interface. Nat. Commun. *11*, 6115. 10.1038/s41467-020-19946-9.

27. Lee, J., Ozden, I., Song, Y.-K., and Nurmikko, A. V. (2015). Transparent intracortical microprobe array for simultaneous spatiotemporal optical stimulation and multichannel electrical recording. Nat. Methods *12*, 1157–1162. 10.1038/nmeth.3620.

28. Kampasi, K., English, D.F., Seymour, J., Stark, E., McKenzie, S., Vöröslakos, M., Buzsáki, G., Wise, K.D., and Yoon, E. (2018). Dual color optogenetic control of neural populations

using low-noise, multishank optoelectrodes. Microsystems Nanoeng. *4*, 10. 10.1038/s41378-018-0009-2.

29. Vöröslakos, M., Kim, K., Slager, N., Ko, E., Oh, S., Parizi, S.S., Hendrix, B., Seymour, J.P., Wise, K.D., Buzsáki, G., et al. (2022). HectoSTAR μLED Optoelectrodes for Large-Scale, High - Precision In Vivo Opto - Electrophysiology. Adv. Sci. *9*, 2105414. 10.1002/advs.202105414.
30. Wu, T., Sher, C.-W., Lin, Y., Lee, C.-F., Liang, S., Lu, Y., Huang Chen, S.-W., Guo, W., Kuo, H.-C., and Chen, Z. (2018). Mini-LED and Micro-LED: Promising Candidates for the Next Generation Display Technology. Appl. Sci. *8*, 1557. 10.3390/app8091557.
31. Chang, W., Kim, J., Kim, M., Lee, M.W., Lim, C.H., Kim, G., Hwang, S., Chang, J., Min, Y.H., Jeon, K., et al. (2023). Concurrent self-assembly of RGB microLEDs for next-generation displays. Nature *617*, 287–291. 10.1038/s41586-023-05889-w.
32. Kang, C.-M., Kang, S.-J., Mun, S.-H., Choi, S.-Y., Min, J.-H., Kim, S., Shim, J.-P., and Lee, D.-S. (2017). Monolithic integration of AlGaInP-based red and InGaN-based green LEDs via adhesive bonding for multicolor emission. Sci. Rep. *7*, 10333. 10.1038/s41598-017-11239-4.
33. Scholvin, J., Kinney, J.P., Bernstein, J.G., Moore-Kochlacs, C., Kopell, N., Fonstad, C.G., and Boyden, E.S. (2016). Close-Packed Silicon Microelectrodes for Scalable Spatially Oversampled Neural Recording. IEEE Trans. Biomed. Eng. *63*, 120–130. 10.1109/TBME.2015.2406113.

34. Khodagholy, D., Gelinas, J.N., Thesen, T., Doyle, W., Devinsky, O., Malliaras, G.G., and Buzsáki, G. (2015). NeuroGrid: recording action potentials from the surface of the brain. Nat. Neurosci. *18*, 310–315. 10.1038/nn.3905.

35. Qiang, Y., Artoni, P., Seo, K.J., Culaclii, S., Hogan, V., Zhao, X., Zhong, Y., Han, X., Wang, P.-M., Lo, Y.-K., et al. (2018). Transparent arrays of bilayer-nanomesh microelectrodes for simultaneous electrophysiology and two-photon imaging in the brain. Sci. Adv. *4*, eaat0626. 10.1126/sciadv.aat0626.

36. Petersen, C.C.H. (2019). Sensorimotor processing in the rodent barrel cortex. Nat. Rev. Neurosci. *20*, 533–546. 10.1038/s41583-019-0200-y.

37. Feldmeyer, D. (2012). Excitatory neuronal connectivity in the barrel cortex. Front. Neuroanat. *6*, 24. 10.3389/fnana.2012.00024.

38. Lefort, S., Tomm, C., Floyd Sarria, J.-C., and Petersen, C.C.H. (2009). The Excitatory Neuronal Network of the C2 Barrel Column in Mouse Primary Somatosensory Cortex. Neuron *61*, 301–316. 10.1016/j.neuron.2008.12.020.

39. Klapoetke, N.C., Murata, Y., Kim, S.S., Pulver, S.R., Birdsey-Benson, A., Cho, Y.K., Morimoto, T.K., Chuong, A.S., Carpenter, E.J., Tian, Z., et al. (2014). Independent optical excitation of distinct neural populations. Nat. Methods *11*, 338–346. 10.1038/nmeth.2836.

40. Govorunova, E.G., Sineshchekov, O.A., Janz, R., Liu, X., and Spudich, J.L. (2015). Natural light-gated anion channels: A family of microbial rhodopsins for advanced optogenetics. Science *349*, 647–650. 10.1126/science.aaa7484.

41. Park, S.-I., Xiong, Y., Kim, R.-H., Elvikis, P., Meitl, M., Kim, D.-H., Wu, J., Yoon, J., Yu, C.-J., Liu, Z., et al. (2009). Printed Assemblies of Inorganic Light-Emitting Diodes for

Deformable and Semitransparent Displays. Science *325*, 977–981. 10.1126/science.1175690.

42. Mao, D., Li, N., Xiong, Z., Sun, Y., and Xu, G. (2019). Single-Cell Optogenetic Control of Calcium Signaling with a High-Density Micro-LED Array. iScience *21*, 403–412. 10.1016/j.isci.2019.10.024.
43. Liu, X., Ren, C., Lu, Y., Liu, Y., Kim, J.-H., Leutgeb, S., Komiyama, T., and Kuzum, D. (2021). Multimodal neural recordings with Neuro-FITM uncover diverse patterns of cortical–hippocampal interactions. Nat. Neurosci. *24*, 886–896. 10.1038/s41593-021-00841-5.
44. Sun, F., Xiong, Z., Park, J., and Xu, G. (2021). Close-Packed PEDOT:PSS-Coated Graphene Microelectrodes for High-Resolution Interrogation of Neural Activity. IEEE Trans. Electron Devices *68*, 3080–3086. 10.1109/TED.2021.3074353.
45. Lee, H.C., Gaire, J., Roysam, B., and Otto, K.J. (2018). Placing sites on the edge of planar silicon microelectrodes enhances chronic recording functionality. IEEE Trans. Biomed. Eng. *65*, 1245-1255. 10.1109/TBME.2017.2715811.
46. Vecchia, D., Beltramo, R., Vallone, F., Chéreau, R., Forli, A., Molano-Mazón, M., Bawa, T., Binini, N., Moretti, C., Holtmaat, A., et al. (2020). Temporal Sharpening of Sensory Responses by Layer V in the Mouse Primary Somatosensory Cortex. Curr. Biol. *30*, 1589-1599.e10. 10.1016/j.cub.2020.02.004.
47. Marblestone, A.H., Zamft, B.M., Maguire, Y.G., Shapiro, M.G., Cybulski, T.R., Glaser, J.I., Amodei, D., Stranges, P.B., Kalhor, R., Dalrymple, D.A., et al. (2013). Physical principles for scalable neural recording. Front. Comput. Neurosci. *7*, 137. 10.3389/fncom.2013.00137.

48. Pluta, S., Naka, A., Veit, J., Telian, G., Yao, L., Hakim, R., Taylor, D., and Adesnik, H. (2015). A direct translaminar inhibitory circuit tunes cortical output. Nat. Neurosci. *18*, 1631–1640. 10.1038/nn.4123.

49. English, D.F., McKenzie, S., Evans, T., Kim, K., Yoon, E., and Buzsski, G. (2017). Pyramidal Cell-Interneuron Circuit Architecture and Dynamics in Hippocampal Networks. Neuron *95*, 505-520. 10.1016/j.neuron.2017.09.033.

50. Hoffman, B.U., Baba, Y., Griffith, T.N., Mosharov, E. V., Woo, S.-H., Roybal, D.D., Karsenty, G., Patapoutian, A., Sulzer, D., and Lumpkin, E.A. (2018). Merkel Cells Activate Sensory Neural Pathways through Adrenergic Synapses. Neuron *100*, 1401-1413.e6. 10.1016/j.neuron.2018.10.034.

51. Jovanovic, V., Fishbein, A.R., de la Mothe, L., Lee, K.-F., and Miller, C.T. (2022). Behavioral context affects social signal representations within single primate prefrontal cortex neurons. Neuron *110*, 1318-1326.e4. 10.1016/j.neuron.2022.01.020.

52. Senzai, Y., Fernandez-Ruiz, A., and Buzsáki, G. (2019). Layer-Specific Physiological Features and Interlaminar Interactions in the Primary Visual Cortex of the Mouse. Neuron *101*, 500-513.e5. 10.1016/j.neuron.2018.12.009.

53. Yu, J., Hu, H., Agmon, A., and Svoboda, K. (2019). Recruitment of GABAergic Interneurons in the Barrel Cortex during Active Tactile Behavior. Neuron *104*, 412-427.e4. 10.1016/j.neuron.2019.07.027.

54. Peyrache, A., and Destexhe, A. (2019). Electrophysiological monitoring of inhibition in mammalian species, from rodents to humans. Neurobiol. Dis. *130*, 104500. 10.1016/j.nbd.2019.104500.

55. Laboy-Juárez, K.J., Ahn, S., and Feldman, D.E. (2019). A normalized template matching method for improving spike detection in extracellular voltage recordings. Sci. Rep. *9*, 12087. 10.1038/s41598-019-48456-y.

56. Diamond, M.E., von Heimendahl, M., Knutsen, P.M., Kleinfeld, D., and Ahissar, E. (2008). "Where" and "what" in the whisker sensorimotor system. Nat. Rev. Neurosci. *9*, 601–612. 10.1038/nrn2411.

57. Hong, Y.K., Lacefield, C.O., Rodgers, C.C., and Bruno, R.M. (2018). Sensation, movement and learning in the absence of barrel cortex. Nature *561*, 542–546. 10.1038/s41586-018-0527-y.

58. Jang, H.J., Chung, H., Rowland, J.M., Richards, B.A., Kohl, M.M., and Kwag, J. (2020). Distinct roles of parvalbumin and somatostatin interneurons in gating the synchronization of spike times in the neocortex. Sci. Adv. *6*, eaay5333. 10.1126/sciadv.aay5333.

59. Tremblay, R., Lee, S., and Rudy, B. (2016). GABAergic Interneurons in the Neocortex: From Cellular Properties to Circuits. Neuron *91*, 260–292. 10.1016/j.neuron.2016.06.033.

60. Xu, H., Jeong, H.-Y., Tremblay, R., and Rudy, B. (2013). Neocortical Somatostatin-Expressing GABAergic Interneurons Disinhibit the Thalamorecipient Layer 4. Neuron *77*, 155–167. 10.1016/j.neuron.2012.11.004.

61. Urban-Ciecko, J., and Barth, A.L. (2016). Somatostatin-expressing neurons in cortical networks. Nat. Rev. Neurosci. *17*, 401–409. 10.1038/nrn.2016.53.

62. Ding, D., Lu, Y., Zhao, R., Liu, X., De-Eknamkul, C., Ren, C., Mehrsa, A., Komiyama, T., and Kuzum, D. (2020). Evaluation of Durability of Transparent Graphene Electrodes Fabricated on Different Flexible Substrates for Chronic In Vivo Experiments. IEEE Trans. Biomed. Eng. *67*, 3203–3210. 10.1109/TBME.2020.2979475.

63. Kim, B.J., and Meng, E. (2016). Review of polymer MEMS micromachining. J. Micromechanics Microengineering *26*, 013001. 10.1088/0960-1317/26/1/013001.

64. Choi, H.W., Liu, C., Gu, E., McConnell, G., Girkin, J.M., Watson, I.M., and Dawson, M.D. (2004). GaN micro-light-emitting diode arrays with monolithically integrated sapphire microlenses. Appl. Phys. Lett. *84*, 2253–2255. 10.1063/1.1690876.

65. Bi, X., Xie, T., Fan, B., Khan, W., Guo, Y., and Li, W. (2016). A Flexible, Micro-Lens-Coupled LED Stimulator for Optical Neuromodulation. IEEE Trans. Biomed. Circuits Syst. *10*, 972–978. 10.1109/TBCAS.2016.2599406.

66. Won, S.M., Cai, L., Gutruf, P., and Rogers, J.A. (2023). Wireless and battery-free technologies for neuroengineering. Nat. Biomed. Eng. *7*, 405–423. 10.1038/s41551-021-00683-3.

67. Greco, G., Iucolano, F., and Roccaforte, F. (2016). Ohmic contacts to Gallium Nitride materials. Appl. Surf. Sci. *383*, 324–345. 10.1016/j.apsusc.2016.04.016.

68. Woolsey, T.A., and Van der Loos, H. (1970). The structural organization of layer IV in the somatosensory region (S I) of mouse cerebral cortex. Brain Res. *17*, 205–242. 10.1016/0006-8993(70)90079-X.

69. Tang, Y., Benusiglio, D., Lefevre, A., Hilfiger, L., Althammer, F., Bludau, A., Hagiwara, D., Baudon, A., Darbon, P., Schimmer, J., et al. (2020). Social touch promotes interfemale communication via activation of parvocellular oxytocin neurons. Nat. Neurosci. *23*, 1125–1137. 10.1038/s41593-020-0674-y.

70. Plexon Inc. (2020). Offline Sorter™: Offline Neural Spike Sorting Software User Guide Version 4.5.0, June.

71. Dworak, B.J., and Wheeler, B.C. (2009). Novel MEA platform with PDMS microtunnels enables the detection of action potential propagation from isolated axons in culture. Lab Chip *9*, 404–410. 10.1039/B806689B.

72. Sander, J., Ester, M., Kriegel, H.P., and Xu, X. (1998). Density-based clustering in spatial databases: The algorithm GDBSCAN and its applications. Data Min. Knowl. Discov. *2*, 169–194. 10.1023/A:1009745219419.

FIGURE LEGENDS

Figure 1. Design and fabrication of the probe.

(A) A packaged probe with illuminated blue and red LEDs, soldered with reference (REF) and ground (GND) electrodes. Scale bar, 5 mm. (B) A zoom-in view of the probe tip and its detailed dimension. Scale bar, 100 μm. (C) Schematic view of a probe being inserted into the mouse somatosensory cortex. Its LEDs and MEA are placed across layers IV and V, and surrounded by excitatory (blue triangle) and/or inhibitory (red/green oval) neurons. (D) Simplified fabrication flow.

Figure 2. LED and MEA characterization.

(A and B) V_{LED} vs I_{LED} (left) and P_{LED} vs I_{LED} (right) for 16 blue LED pixels (A) and 16 red LED pixels (B), respectively. Shaded areas represent ±1 S.D. (C) Spatial profile of the pixel output (from a blue LED pixel and its neighboring red LED pixel) at the array surface with I_{LED} = 2 to 10 [5 to 25] μA for the blue [red] LED pixel. (D) Pixel output pulsed with a 10-ms pulse width at 40 Hz for blue (top) and red (bottom) pixels. Blue [red] LED pixels were biased at I_{LED} = 10 [25] μA. (E to G) Electrochemical characterization of the MEA before (black) and after (red) PEDOT: PSS electroplating, including EIS impedance (E) and EIS phase (F) of all 17 electrodes (with the average being highlighted), and CV of a typical electrode measured in the tenth cycle and scanned at 1000 mV/s (G).

Figure 3. Artifact characterization.

(A) The definition of V_{pp} and strategies of artifact suppression. (B) V_{pp} values with one single blue/red LED pixel being pulsed under different artifact suppression strategies. (C) Recording traces with LP filtered, V_{low} adjusted pulsing of one single blue/red LED pixel (aligned to the voltage pulse applied to the LED pixel). Shaded areas represent ±1 S.D. (D) V_{pp} values with LP

filtered, V_{low} adjusted pulsing of different blue/red LED pixels. In (B) and (D), error bars represent ±1 S.D. from all 17 electrodes.

Figure 4. Bi-directional *in vivo* optogenetic electrophysiology across layers IV and V.

(A) A representative recording trace (excluding the 4-ms of data centered at the rising/falling edges of each LED pulse) when 6 red and 6 blue LED pixels were sequentially illuminated and the threshold (red) for spike detection. (B) Sorted spike waveforms during the 14-s pulsing periods of red (i) and blue (ii) LEDs were aligned by their negative peaks with their average shown in black. (C) Positions of illuminated LED pixels. (D) Raster plots of 7 trials from a representative electrode (green highlight in (C)). Red [blue] windows represent the red [blue] LED pulses. (E) PSTH summed from all 112 trials (16 active electrodes with 7 trials each). (F) Spike count across MEA. Data were collected from the [0, 100 ms] window in (D) and summed from 7 trials of each electrode. (G) Percentage changes of the spike count compared to those from the [-100 ms, 0] window (before LED pulsing).

Figure 5. Layer-specific bi-directional optogenetic control over whisker-evoked neural activity.

(A) Positions of illuminated LED pixels combining with whisker stimulations. (B) Raster plots of 7 trials from a representative electrode (green highlight in (A)). Green windows represent the whisker pulses, red [blue] windows represent the red [blue] LED pulses. (C) PSTH summed from all 112 trials (16 active electrodes with 7 trials each). (D) Spike count across the MEA. Data were collected from the [0, 100 ms] window in (B) and summed from 7 trials of each electrode. (E) Percentage changes of the spike count in (D) compared to the whisker-stimulation-alone experiment. (F and G) Percentage changes of the spike count (compared to the whisker-stimulation-alone experiment) by pulsing 6/3 red (R in (F)) or 6 blue (B in (G)) LED pixels located

in layer IV or V. Error bars represent ±1 S.D from 16 active electrodes; *** $p < 0.001$, n.s. $p > 0.05$ based on Student's *t*-test.

Figure 1. Design and fabrication of the probe.

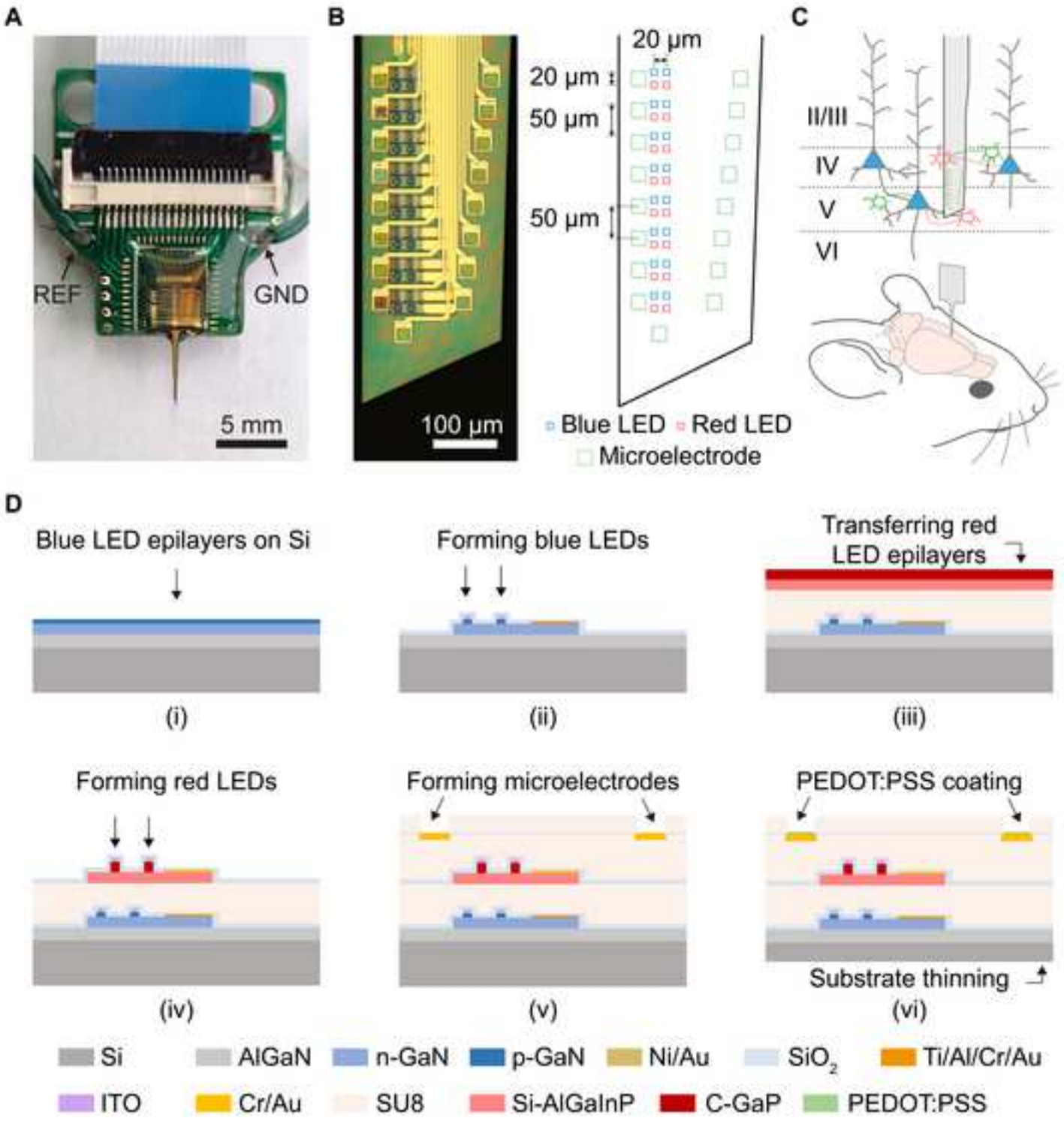

Figure 2. LED and MEA characterization.

Click here to access/download;Figure;Figure-2.tif

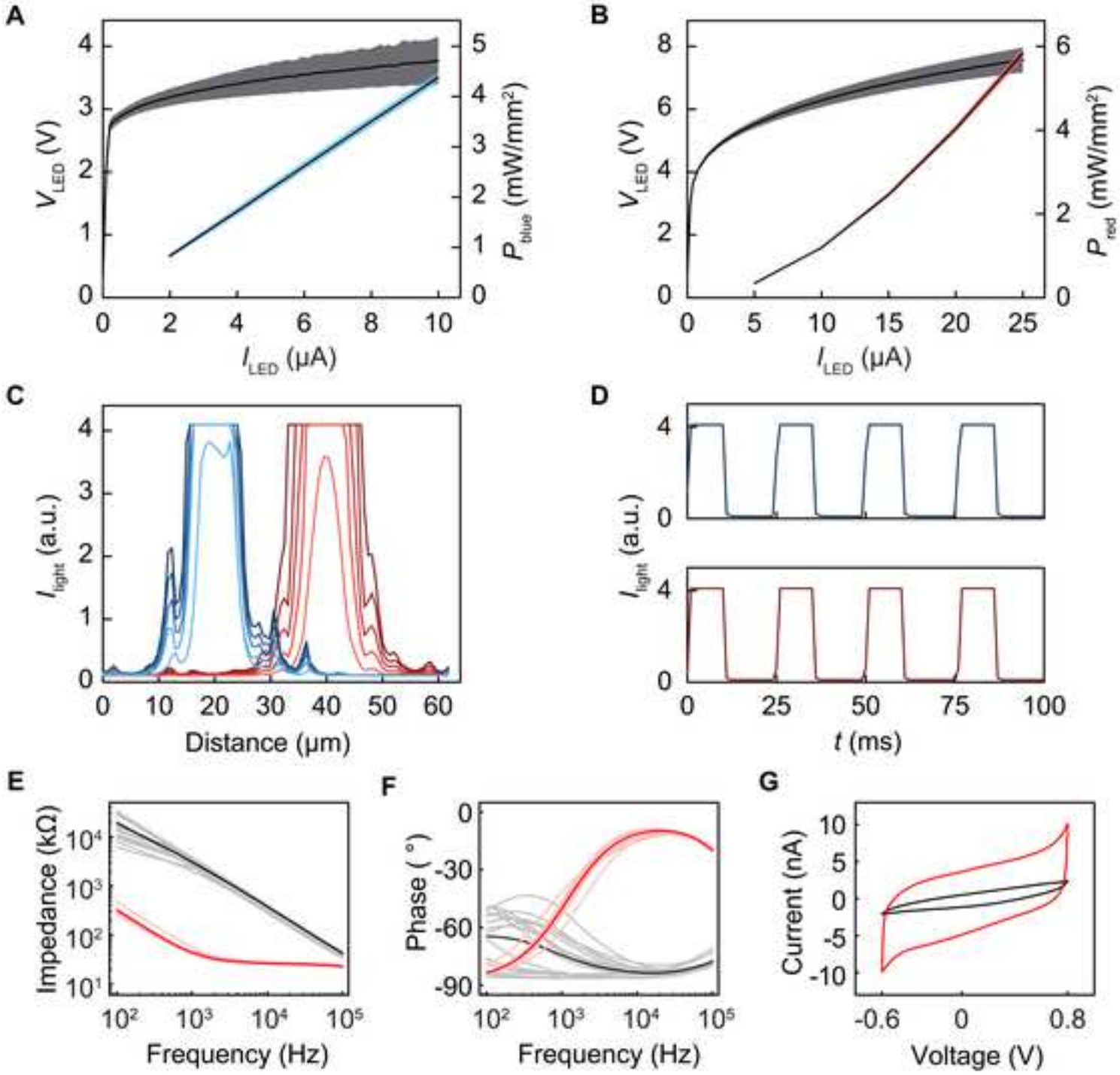

Figure 3. Artifact characterization.

Click here to access/download;Figure;Figure-3.tif

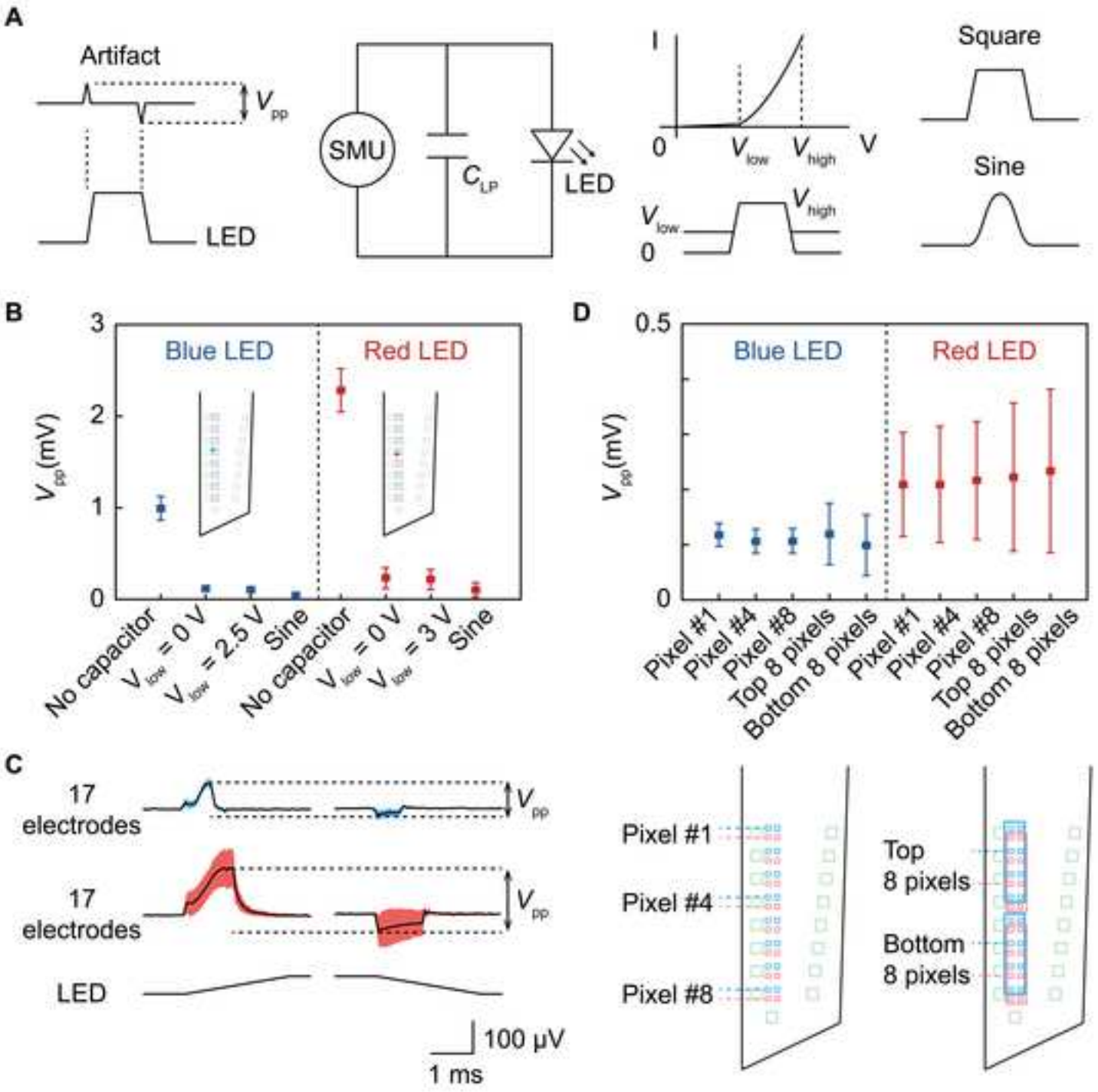

Figure 4. Bi-directional in vivo optogenetic electrophysiology across layers IV and V.

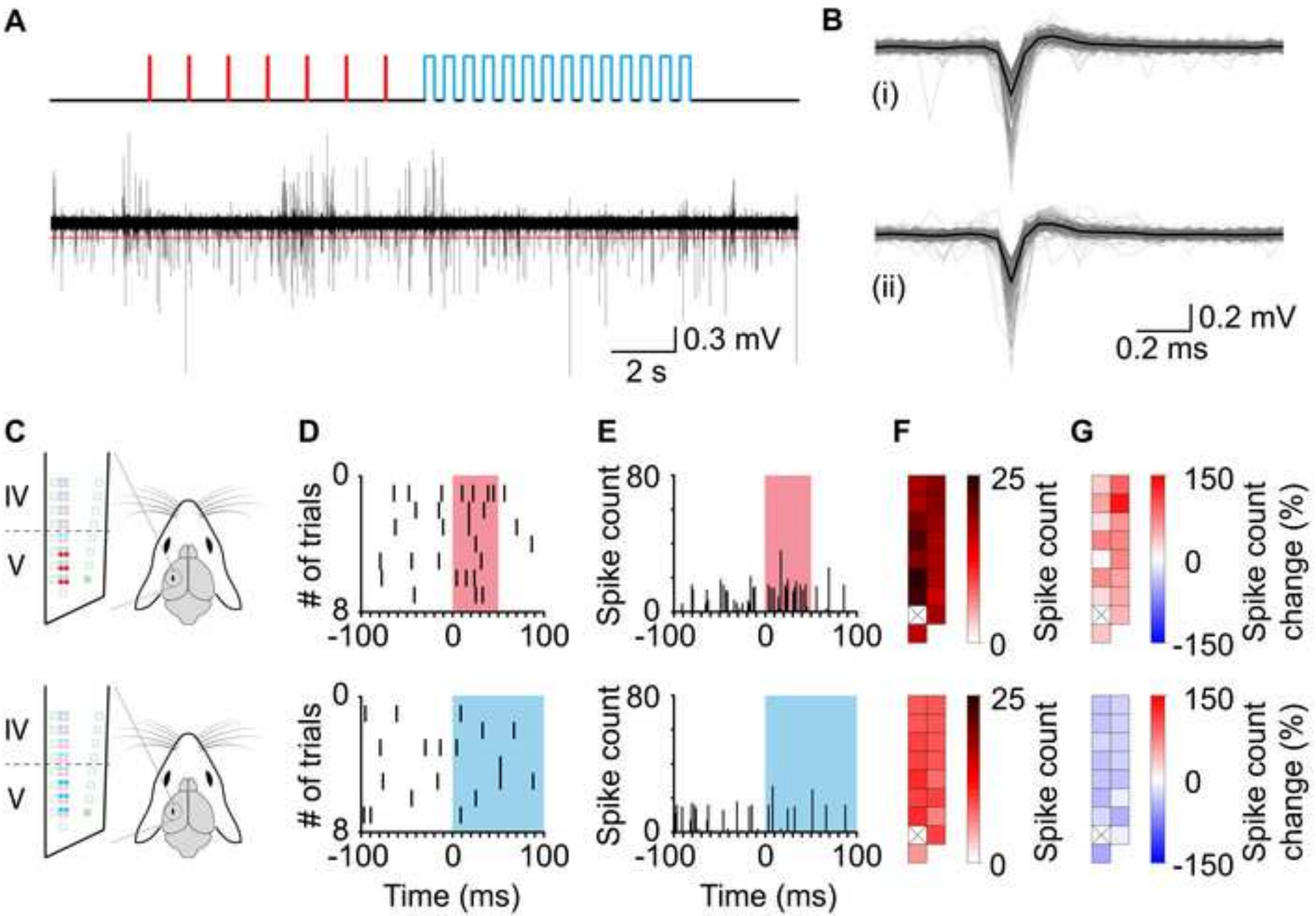

Figure 5. Layer-specific bi-directional optogenetic control over whisker-evoked neural activity.

Click here to access/download;Figure;Figure-5.tif